Deviation from the Normal Mode Expansion in a Coupled Graphene-Nanomechanical System

Cornelia Schwarz, Benjamin Pigeau, Laure Mercier de Lépinay, Aurélien G. Kuhn, Dipankar Kalita, Nedjma Bendiab, Laëtitia Marty, Vincent Bouchiat, and Olivier Arcizet*

Institut Néel, Université Grenoble Alpes-CNRS:UPR2940, 38042 Grenoble, France

(Received 3 December 2015; revised manuscript received 14 November 2016; published 29 December 2016)

A significant deviation from the normal mode expansion is observed in the optomechanically measured thermal noise of a graphene membrane suspended on a silicon nitride nanoresonator. This deviation is due to the heterogeneous character of mechanical dissipation over the spatial extent of coupled eigenmodes, which is tuned through an avoided anticrossing. We demonstrate that the fluctuation-dissipation theorem permits a proper evaluation of the thermal noise of the coupled nanomechanical system. Since a good spatial homogeneity is delicate to ensure at the nanoscale, this approach is fundamental to correctly describing the thermal noise of nanomechanical systems which ultimately impact their sensing capacity.

DOI: 10.1103/PhysRevApplied.6.064021

I. INTRODUCTION

Nanomechanical oscillators are routinely used in fundamental and applied physics [1,2] as ultrasensitive force or mass sensors due to their increased sensitivity to their environment. The understanding of dissipation at the nanoscale is the key ingredient towards extreme sensitivity operation. Among others, carbon-based nanoresonators and alternative 2D materials [3] have revolutionized the field of nanomechanics [4–14] by pushing the oscillator dimensions down to a single atomic layer. The extreme sensitivities achieved are ultimately limited by the thermal noise of the nanoresonators, which underlines the importance of correctly understanding and describing their Brownian motion. The thermal noise of a vibrating nanomechanical system is commonly described using the normal mode expansion, which assumes that each eigenmode is driven by an independent fluctuating Langevin force, presenting no correlation with other eigenmodes. However, this intuitive description only holds when the mechanical dissipation is homogeneously distributed in the system [15–17]. Otherwise, inhomogeneous damping can create dissipative coupling between eigenmodes, leading to a violation of their assumed independence. Such deviations, which have been reported on macroscopic devices [18,19], are expected to be extremely important in nanomechanical systems since it becomes increasingly difficult to ensure and even measure a good spatial homogeneity over the entire nanosystem as its size is decreased. However, no deviations from the normal mode expansion have been observed at the nanoscale to date, despite the large variety of nanoresonators investigated.

In this article, we report on the deviation from the normal mode expansion in the optomechanically measured thermal noise of a nanomechanical arrangement made of a suspended graphene monolayer coupled to a silicon nitride nanomembrane which supports the graphene resonator. To fully explore the deviation from the normal mode expansion, we exploit the inertial coupling between both nanoresonators: upon temperature-controlled tunable hybridization, the coupled eigenmodes become spatially delocalized on the two subsystems whose intrinsic mechanical damping rates differ by 2 orders of magnitude. In this situation with strong coupling between the two nanoresonators, the damping homogeneity is, therefore, no longer maintained, which results in a pronounced deviation from the normal mode expansion that we report on and analyze. Then we measure the local mechanical susceptibility of the coupled nanomechanical system and prove that the fluctuation-dissipation theorem still holds across the entire observed anticrossing—that is, for both homogeneously and heterogeneously distributed mechanical damping.

These considerations are essential for correctly describing nanomechanical systems affected by inhomogeneous damping and point out the importance of having access to the local mechanical susceptibility to correctly estimate the thermal noise of complex nanomechanical systems.

II. SAMPLE PREPARATION

Our nanomechanical system is a fully suspended single-layer graphene sheet deposited on a square window opened in a Si_3N_4 nanoresonator, itself supported on an opened silicon wafer (see Fig. 1), which allows a dual optical access from both sides. It is obtained [see the Supplemental Material (SM) [20]] by transfer in the liquid phase of a monolayer, polycrystalline graphene grown by CVD on Cu [21,22] and suspended over up to $25 \times 25\ \mu m^2$ on a prepatterned stoichiometric Si_3N_4 membrane which is 500 nm thick and 100 μm wide.

*olivier.arcizet@neel.cnrs.fr

The used substrate is a silicon wafer coated on both sides with plasma-sputtered low-stress Si_3N_4 thin films of 500 nm thickness. Large windows of about 100×150 μm are defined using laser lithography on the wafer back side, while smaller square windows (4–25 μm sized) are defined on the top surface, centered above the bottom windows. The silicon nitride is etched away by reactive-ion etching in a SF_6 plasma. In order to permit optical transmission through the sample, and thus optical access from both sides, the silicon is subsequently etched away through the windows opened in the silicon nitride layers in a KOH solution. This etching away results in suspended silicon nitride membranes with predefined holes, as shown in Fig. 1 and the SM [20]. The graphene is grown on a copper foil by chemical vapor deposition from a methane precursor to form a continuous layer [21]. The monolayer graphene is covered by a spin-coated resist support layer (PMMA) and the copper is etched away in an ammonium persulfate solution. The graphene is then transferred onto the pre-patterned substrate. After removal of the PMMA layer in acetone and rinsing in isopropanol, the sample is dried in a supercritical carbon dioxide dryer to protect it from strong surface-tension forces that can be exerted by drying liquid droplets. The quality of the suspended graphene and the low levels of doping and residual strain are verified and estimated [23] using confocal micro-Raman mapping; see the SM [20].

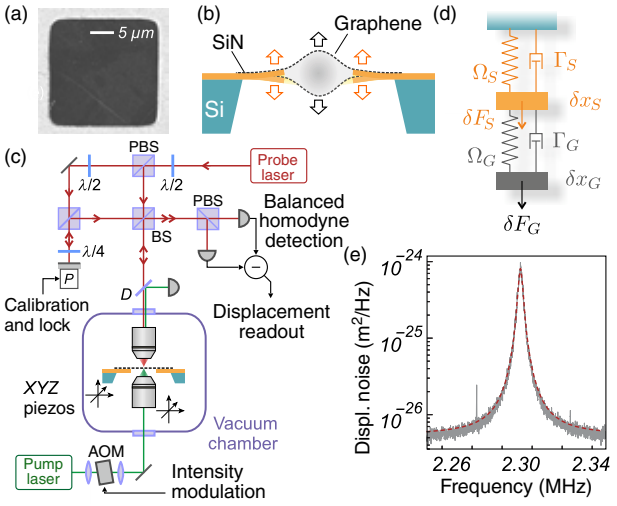

FIG. 1. The experimental setup. (a) SEM of a 20×20 μm^2 suspended CVD-grown graphene monolayer supported on a 300-nm-thick SiN nanomembrane, as sketched in (b). (c) Experimental setup. A balanced homodyne detection measures the phase fluctuations of the probe-laser field reflected by the sample and monitors its position fluctuations. A second counterpropagating pump-laser beam can be intensity modulated to optomechanically drive the coupled nanoresonators. The experiment is performed at pressures below 10^{-3} mbar. (d) Model describing the inertially coupled nanoresonators. (e) Thermal noise of a graphene membrane. The sharp peaks on each side are weakly coupled SiN eigenmodes.

III. THE EXPERIMENTAL SETUP

A 633-nm probe laser is focused on the graphene resonator with a high numerical-aperture objective (whose optical waist approximately equals 400 nm). The weak reflected beam constitutes the signal arm of a balanced homodyne detection [24] [see Fig. 1(c) and the SM [20]]. The sample is mounted vertically on an *XYZ* piezoelectric stage ($100 \times 100 \times 100$ μm scan range) permitting a precise positioning with respect to the probe-laser beam, which is fixed in space in order to ensure a stable operation of the interferometer. The long working distances (4 mm) and large numerical apertures (0.75) of the microscope objectives employed permit us to focus the laser beams down to optical waists of approximately 330 nm with half focusing angles approximately equal to 45°. This angle is smaller than the KOH chemical-etching angle of silicon (54°) so that a full laser-beam transmission is preserved all over the graphene membrane. The experiment is conducted in a vacuum chamber to suppress air damping, which limits the oscillators' quality factors. Static pressures below 0.01 mbar can be maintained over several days.

The interferometer permits a shot-noise-limited readout of the membrane's thermal noise, with injected optical powers ranging from 1 to 100 μW. A fast piezoelectric element driving the local oscillator mirror permits a robust calibration of the interferometer, particularly insensitive to spatial drifts or reflectivity variations due to nonhomogeneous graphene properties (wrinkles or grain boundaries). Reflectivities in the 1%–10% range are measured on monolayers depending on the level of contaminants. A typical calibrated-displacement noise spectrum is shown in Fig. 1. Its reproduction at varying optical powers permits us to verify the absence of optical backaction (see the SM [20]). The uncoupled graphene resonators present fundamental eigenmodes in the 1–10 MHz range, with quality factors from 10 to 500 in vacuum and effective masses ranging from 10^{-16} to 10^{-14} kg. Operating with fully transmitting systems permits the suppression of additional cavity effects [25] which could complicate the noise thermometry. The spatial profile of graphene eigenmodes can be mapped by probing thermal-noise spectra at varying positions on the graphene membrane; see the SM [20]. The slight elliptical structure and the frequency splitting observed on higher-order modes reflects the presence of a residual 20-MPa stress along the diagonal direction [26,27], attributed to the graphene transfer process. Also visible on the thermal-noise spectrum are sharp peaks corresponding to higher-order eigenmodes of the Si_3N_4 nanomembrane, whose fundamental mode oscillates at around 100 kHz. They present larger quality factors (above 1000) but higher masses, on the order of 10^{-12} kg. In the

following, we investigate the thermal noise of the coupled system.

IV. HYBRIDIZATION OF GRAPHENE EIGENMODES

In order to tune the eigenfrequencies, we exploit the partial absorption of a second laser beam at 532 nm focused down to an optical waist of ≃300 nm, spatially superimposed on the probe beam and injected from the opposite side of the sample. It generates a slight temperature increase which is almost nondetectable in the Brownian temperature [see Fig. 2(e)] but is sufficient to significantly thermally tune the graphene eigenfrequency. A clear hybridization between both the graphene and Si_3N_4 eigenmodes is shown in Fig. 2(b), where a pronounced frequency anticrossing can be seen, as well as a modification of the mechanical damping rates. Such signatures are fingerprints of strong

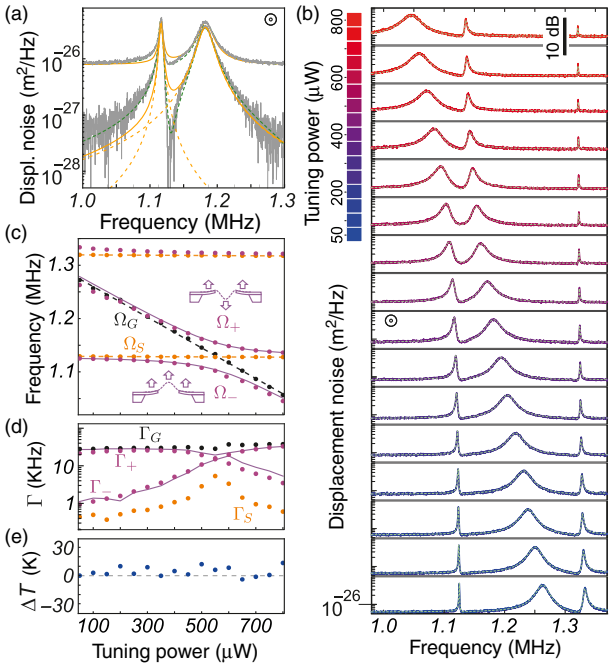

FIG. 2. Thermal noise of the hybridized eigenmodes. (a) Thermal noise of the coupled nanomechanical system measured in the middle of the graphene membrane ($S_{\delta x_G}[\Omega]$) when tuned to an anticrossing region by adjusting the pump intensity (400 μW). Lower traces are obtained after numerical background substraction. The solid lines are the best fits derived employing the normal mode expansion. The dashed green lines are fits using expression (4). (b) Spectra measured through the anticrossing for increasing tuning laser powers. The dashed lines are fits using Eq. (4) with the fitting parameters $\Omega_{S,G}$, $\Gamma_{S,G}$ reported in (c),(d) using $\mu = 0.002$. The purple disks represent the measured coupled eigenfrequencies $\Omega_\pm/2\pi$, and the solid lines are deduced from Eq. (3). (d) A similar analysis for damping rates $\Gamma_\pm/2\pi$. (e) Relative Brownian temperature variation deduced from the fits.

dual-mode coupling [28], which can also affect the force sensitivity [29–31].

The modelization of our inertially coupled nanomechanical system is based on cascaded mechanical oscillators [15,16], as sketched in Fig. 1(d). Their vibrations δx_G and δx_S around the rest positions are coupled through

$$\begin{aligned}\delta\ddot{x}_G &= -\Omega_G^2(\delta x_G - \delta x_S) - \Gamma_G(\delta\dot{x}_G - \delta\dot{x}_S) + \delta F_G/M_G \\ \delta\ddot{x}_S &= -\Omega_S^2\delta x_S - \Gamma_S\delta\dot{x}_S + \mu\Omega_G^2(\delta x_G - \delta x_S) \\ &\quad + \mu\Gamma_G(\delta\dot{x}_G - \delta\dot{x}_S) + \delta F_S/M_S, \end{aligned} \tag{1}$$

where $\Omega_{G,S}/2\pi$ ($\Gamma_{G,S}$) are the uncoupled frequencies (damping rates). δF_G is an external force applied on the graphene membrane and M_G the graphene effective mass at the measurement location [17], while $\mu \equiv M_G/M_S$ parametrizes the hybridization strength. Depending on the graphene and Si_3N_4 membrane geometries which govern the vibration-mode spectrum and their spatial profiles, anticrossings with varying strength can be observed (see the SM [20]). Intuitively, if graphene is positioned at a node of the membrane eigenmode, their hybridization will be reduced. In the Fourier domain, we have $\begin{pmatrix}\delta x_G \\ \delta x_S\end{pmatrix} = \boldsymbol{\chi}[\Omega]\cdot\begin{pmatrix}\delta F_G \\ \mu\delta F_S\end{pmatrix}$, using $\delta x_i[\Omega] \equiv \int_{\mathbb{R}} dt e^{i\Omega t}\delta x_i(t)$. The dynamical matrix $\boldsymbol{\chi}[\Omega]^{-1}$ is

$$\begin{pmatrix} \chi_G^{-1} & M_G\Omega^2 - \chi_G^{-1} \\ \mu(M_G\Omega^2 - \chi_G^{-1}) & \mu(\chi_S^{-1} + \chi_G^{-1} + M_G\Omega^2) \end{pmatrix}, \tag{2}$$

where we use the uncoupled mechanical susceptibilities $\chi_{G,S} \equiv M_{G,S}^{-1}(\Omega_{G,S}^2 - \Omega^2 - i\Omega\Gamma_{G,S})^{-1}$. Diagonalizing the restoring-force matrix $M_G^{-1}\boldsymbol{\chi}[0]^{-1}$ yields the new eigenfrequencies $\Omega_\pm/2\pi$ of the coupled system:

$$\Omega_\pm^2 \equiv \frac{(1+\mu)\Omega_G^2 + \Omega_S^2}{2} \pm \frac{\sqrt{(\Omega_S^2 - (1+\mu)\Omega_G^2)^2 + 4\mu\Omega_G^2\Omega_S^2}}{2}. \tag{3}$$

When $\mu \ll 1$, the minimum relative-frequency splitting amounts to $\sqrt{\mu}$, corresponding to a canonically defined coupling strength of $g = \Omega_G\sqrt{\mu}$ [28]. Depending upon the sample geometry, a large variety of coupling strengths can be observed, up to 200 kHz, largely entering the so-called strong-coupling regime ($g > \Gamma_S, \Gamma_G$). The experimentally measured coupled eigenfrequencies are shown in Fig. 2(c) for increasing pump-laser powers. They can be well fitted using Eq. (3) and a linear pump-power dependence for the uncoupled graphene and Si_3N_4 eigenfrequencies of -284 Hz/μW and -2 Hz/μW, respectively. The latter corresponds to a maximum static heating of the Si_3N_4 nanoresonator estimated at the level of ≃1 K [32]. Using the experimentally measured heat diffusion coefficient of

$5 \times 10^{-6} m^2/s$ (see the SM [20]), the thermal heat resistance of graphene is numerically estimated at 0.25 K per microwatt absorbed. The effective mechanical damping rates $\Gamma_\pm$ of the coupled modes can be roughly estimated using the FWHM of the thermal-noise spectra [see Fig. 2(d)] and then used to extrapolate the uncoupled damping rates (see the SM [20]).

V. VIOLATION OF THE NORMAL MODE EXPANSION

Meanwhile, a striking feature can be seen in the displacement noise spectra shown in Fig. 2: a characteristic peak asymmetry and a sharp noise minimum between both eigenmodes are clearly visible in the anticrossing region. These spectra cannot be fitted with two independent mechanical thermal-noise spectra [see Fig. 2(a)] with a deviation larger than 10 dB observed in the vicinity of Ω_S. Therefore, the measured thermal noise cannot be described by two eigenmodes driven with independent Langevin forces, which reveals the violation of the normal mode expansion. As illustrated in Fig. 3, this violation is a consequence of the spatial inhomogeneity of damping rates across the system: acoustic vibrations are more efficiently damped in graphene than in Si_3N_4. When the eigenmodes become hybridized, their spatial profiles are delocalized

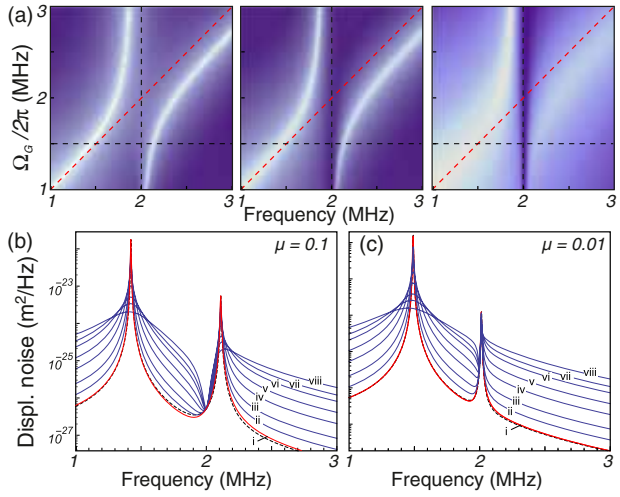

FIG. 3. Role of damping heterogeneity. (a) Numerical simulations of thermal-noise spectra deduced from the model (see the SM [20]) for varying uncoupled graphene frequency Ω_G and different graphene damping rates. From left to right, $\Gamma_G/2\pi = 5$, 50, and 500 kHz ($\Omega_S/2\pi = 2$ MHz, $\mu = 0.1$, $\Gamma_S/2\pi = 5$ kHz). (Bottom panels) Thermal-noise spectra calculated with $\Omega_G/2\pi =$ 1.5 MHz for different graphene damping rates [5, 10, 20, 50, 100, 200, 300, and 500 kHz from (i) to (viii)] and respective coupling strength of $\mu = 0.1$ and 0.01 for (b) and (c), respectively. The peak asymmetry and the noise reduction are absent in the case of homogeneous damping (i), and the simulations are well described by a modal expansion (the dashed lines).

over both systems [see the Fig. 2(c) insets], so that mechanical damping becomes inhomogeneous over the eigenmode spatial extension. Thus, the spatial profile of the vibration pattern cannot be stationary anymore since it is nonhomogeneously damped and cannot be preserved over time. As such, dissipation is now able to couple eigenmodes, which breaks the fundamental hypothesis required to apply the normal mode expansion [15,17]. When $\Omega_G = \Omega_S$, the thermal-noise spectral density at the minimum noise frequency is measured at a level approximately $2\Gamma_G/\Gamma_S$ times lower than the prediction of the normal mode expansion; see the SM [20]. The understanding of this deviation is critical for patching the normal mode expansion and working out an analytical description of the system fluctuations.

VI. THERMAL NOISE OF THE HYBRIDIZED NANOMECHANICAL SYSTEM

To properly describe the nanosystem thermal noise, it is necessary to return to the original formulation of the fluctuation-dissipation theorem [15,33]:

$$S_{\delta x_G}[\Omega] = \frac{2k_B T}{|\Omega|}|\mathrm{Im}\chi_{GG}[\Omega]|, \tag{4}$$

which relates the measured displacement noise spectral density to the local mechanical susceptibility χ_{GG}. The latter connects the optomechanically measured deformations of the graphene membrane $\delta x_G[\Omega]$ to the external force δF_G applied on the graphene membrane at the measurement point: $\delta x_G[\Omega] = \chi_{GG}[\Omega]\delta F_G$. First, we pursue the analysis based on the model employed above. Inverting Eq. (2), we obtain

$$\chi_{GG}[\Omega]^{-1} = \chi_G^{-1} - \frac{(\chi_G^{-1} + M_G\Omega^2)^2}{\chi_G^{-1} + \chi_S^{-1} + M_G\Omega^2}, \tag{5}$$

which permits a derivation of the expected thermal noise (see the SM [20]) using Eq. (4). Our experimental results can be well fitted with this model [see Figs. 2(a) and 2(b)] using the fitting parameters which are reported in Figs. 2(c), 2(d), and 2(e). The magnitude of the coupling parameter $\mu = 0.002$ is also in agreement with the ratio of bare effective masses of both nanoresonators. No significant variation in the fitted noise temperature could be detected [see Fig. 2(e)], which places an upper bound of $\simeq$10 K on the maximum temperature increase induced by the tuning laser. This observation is also consistent with the estimated thermal resistance given above and allows us to neglect the role of temperature inhomogeneities in our modelization.

VII. VALIDITY OF THE FLUCTUATION-DISSIPATION THEOREM IN THE COUPLED NANOMECHANICAL SYSTEM

Verifying the validity of the fluctuation-dissipation theorem is essential in order to assess whether the measured

spectra correspond to the thermal noise of the system. Following the principles of linear response theory [33], this verification requires measuring the local mechanical susceptibility χ_{GG} of the coupled nanomechanical system. To do so, we modulate the pump beam intensity by means of an acousto-optic modulator (AOM) and realize response measurements by sweeping the modulation frequency while recording the driven displacement. Both laser spots are carefully superimposed on the graphene membrane to access the local susceptibility; it is worth mentioning that this measurement cannot be realized with electrostatic gate or with piezoelectric actuations since their spatial excitation profile is not localized on the measurement spot. We first verify the linearity of the actuation [see Fig. 4(a)] by varying the optical modulation depth δP over 2 orders of magnitude without modifying the mean pump power (60 μW) to ensure a stable graphene frequency, away from the anticrossings. No deviation from linearity are observed in the driven oscillations up to a maximum amplitude of 1 nm, a few times the monolayer thickness (0.3 nm), so that we perfectly sit in the linear actuation and measurement regime. A typical actuation efficiency of 17 pm/μW is measured, corresponding to an optical force of 540 fN/μW. This value is significantly larger than the radiation-pressure-force contribution of 0.3 fN/μW for a 10% absorption coefficient, which confirms the dominant role of photothermal forces [34,35] in the optical actuation of graphene [25]. The backaction noise resulting from the intensity fluctuations of the shot-noise-limited laser beams can thus be evaluated at the level of $\simeq$0.1 fm/$\sqrt{\text{Hz}}$ for $P_0 = 100$ μW. This value is largely negligible compared to the measured thermal noise, so backaction cancellation [36] and classical noise-squashing mechanisms [37] can be safely excluded while interpreting our results.

Several response measurements are subsequently performed through the anticrossing in the same measurement conditions as in Fig. 2(a) by progressively increasing the pump intensity while maintaining a fixed modulation depth ($\delta P/P_0 = 30\%$). The response curves shown in Fig. 4(c) permit us, once combined with the optical to force conversion factor measured in Fig. 4(a) in the absence of hybridization, to determine the complex local mechanical susceptibility, $\chi_{GG}[\Omega]$, as shown in Fig. 4(d). Its proper determination requires us to take into account the weak residual contribution of the interferometer feedback loop in the measurement span, the transfer function of all photodetectors employed, and the spectral response of the AOM. With this determination, the expected thermal noise can be properly estimated using Eq. (4) and compared to the measured thermal-noise spectrum, as shown in Fig. 4(e). The excellent quantitative agreement found between both measurements all across the hybridization

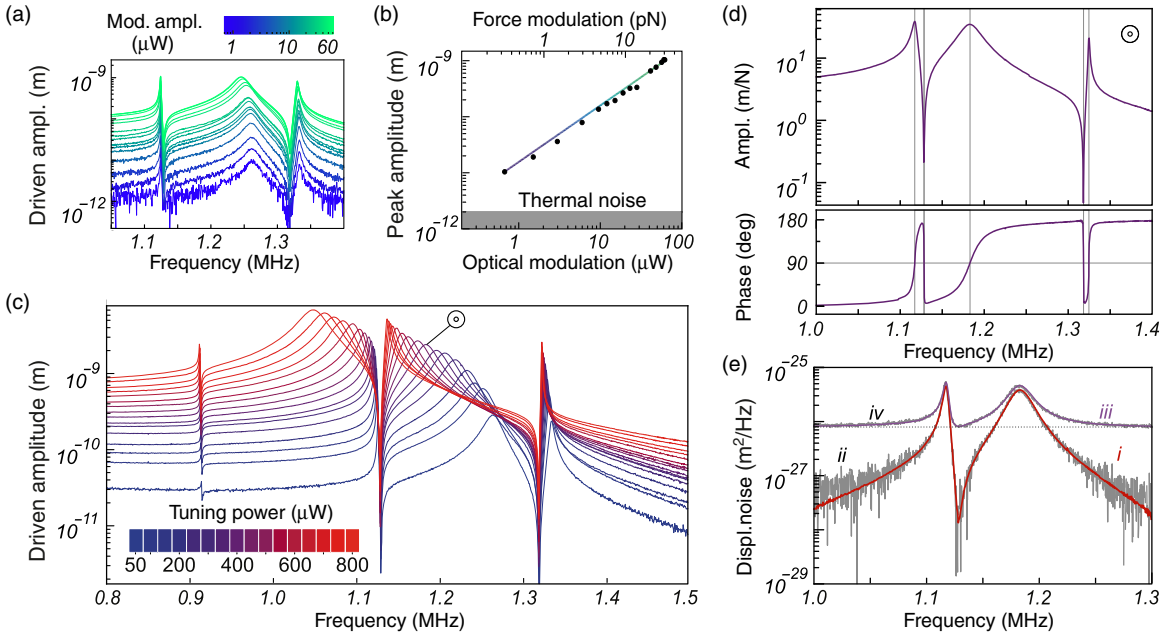

FIG. 4. Optomechanical response of the hybridized nanomechanical system. (a) Optomechanical response obtained by modulating the pump intensity for increasing modulation depths δP with a fixed average tuning power ($P_0 = 60$ μW). (b) Maximum driven displacement reported as a function of δP. The solid line has a slope of 17 μm/W. (c) Optomechanical responses obtained for an increasing optical pump power P_0 (30% modulation strength). (d) Amplitude and phase of the mechanical susceptibility χ_{GG} derived for 400 μW of tuning power. The corresponding thermal-noise spectrum expected using Eq. (4) is reported in (e)(i) and presents a very good agreement with the measured spectrum (ii). The detection noise is included in traces (iii) and (iv). A 30% correction is used here on the optical to the force conversion factor determined in Fig. 4(a) to account for a slight modification of the actuation efficiency between both measurements.

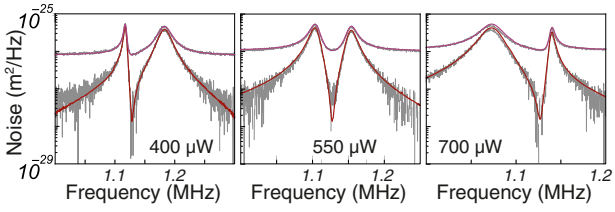

FIG. 5. Probing fluctuation-dissipation theorem validity at different tuning powers while following the same conventions as in Fig. 4(e). Response measurements of Fig. 4 are used to compute the local effective mechanical susceptibility subsequently injected in Eq. (4) and compared to the experimental spectra. For the entire data set, the only free parameter is an overall correction factor (from 0.8 to 1.2) to account for slight drifts in the readout and actuation efficiencies.

(see Fig. 5) demonstrates the validity of the fluctuation-dissipation theorem in our strongly coupled nanomechanical arrangement.

The hybridization dramatically modifies the graphene mechanical response and has an impact on the signal-to-noise ratio (SNR) observed in a force measurement. For a monochromatic force of amplitude δF_G applied in the center of the graphene membrane, the SNR can be expressed as $\mathrm{SNR}[\Omega]/(\mathrm{SNR}_G) = |\mathrm{Im}\,\chi_G^{-1}/\mathrm{Im}\,\chi_{GG}^{-1}|$, where $\mathrm{SNR}_G \equiv \delta F_G^2/2M_G\Gamma_G k_B T$ represents the SNR of the uncoupled graphene alone. As verified experimentally and confirmed with the model (see the SM [20]), the SNR can be improved with respect to the uncoupled graphene resonator in narrow frequency bands in the vicinity of the Si_3N_4 resonance. As already employed with macroscopic devices [19], this approach constitutes a strategy for achieving larger sensitivities in hybrid nanosensors.

VIII. CONCLUSIONS

In this paper, we demonstrate the violation of the normal mode expansion in a multimode nanomechanical system and verify that the fluctuation-dissipation theorem well describes its thermal noise despite the large mass and damping asymmetries. This work underlines the importance of measuring the local mechanical susceptibility of a nanosystem to correctly understand its thermal noise. Since a good sample homogeneity is more delicate to ensure in extremely downsized nanomechanical devices, we anticipate that these deviations will play an important role in the future of nanomechanical sensors. Our observations, realized on inertially coupled nanomechanical oscillators, have a more general reach and are also valid when mechanical modes are externally coupled, such as by optical or electrostatic force-field gradients [8,14,38–44]. Such a fundamental approach could be used for developing alternative force-detection protocols based on multimodal nanosystems. Furthermore, optomechanical cooling is intrinsically responsible for both mode cross-coupling and nonhomogeneous modification of the damping rates when the feedback actuation profile does not perfectly match the vibration profile of the mode of interest. Therefore, our conclusions and our approach should be directly transposed to correctly understand the noise of actively cooled multimode optomechanical systems [38,45–47]. Finally, we emphasize that the coupling mechanism involved here is of a conservative nature in the sense that it does derive from a potential energy.

ACKNOWLEDGMENTS

We warmly thank J. Jarreau, C. Hoarau, E. Eyraud, D. Lepoittevin, B. Fernandez, J. P. Poizat, A. Gloppe, and B. Besga for the experimental and technical assistance. This work is supported by the ANR FOCUS, ERC Starting Grant No. StG-2012-HQ-NOM, the EC Graphene Flagship (Project No. 604391) and by the Laboratoire d'excellence LANEF in Grenoble (ANR-10-LABX-51-01) (CryOptics). C. S. acknowledges funding from the Nanoscience Foundation.

[1] A. N. Cleland, *Foundations of Nanomechanics* (Springer, Heidelberg, 2003).
[2] K. L. Ekinci and M. L. Roukes, Nanoelectromechanical systems, Rev. Sci. Instrum. **76**, 061101 (2005).
[3] A. Castellanos-Gomez, H. S. J. Singh, V. van der Zant, and G. A. Steele, Mechanics of freely-suspended ultrathin layered materials, Ann. Phys. (Berlin) **527**, 27 (2015).
[4] Vera Sazonova, Yuval Yaish, Hande Ustunel, David Roundy, Tomas A. Arias, and Paul L. McEuen, A tunable carbon nanotube electromechanical oscillator, Nature (London) **431**, 284 (2004).
[5] Changyao Chen, Sami Rosenblatt, Kirill I. Bolotin, William Kalb, Philip Kim, Ioannis Kymissis, Horst L. Stormer, Tony F. Heinz, and James Hone, Performance of monolayer graphene nanomechanical resonators with electrical readout, Nat. Nanotechnol. **4**, 861 (2009).
[6] Arend M. Van der Zande, Robert A. Barton, Jonathan S. Alden, Carlos S. Ruiz-Vargas, William S. Whitney, Phi H. Q. Pham, Jiwoong Park, Jeevak M. Parpia, Harold G. Craighead, and Paul L. McEuen, Large-scale arrays of single-layer graphene resonators, Nano Lett. **10**, 4869 (2010).
[7] J. Chaste, A. Eichler, J. Moser, G. Ceballos, R. Rurali, and A. Bachtold, A nanomechanical mass sensor with yoctogram resolution, Nat. Nanotechnol. **7**, 301 (2012).
[8] J. Moser, J. Guttinger, A. Eichler, J. M. Esplandiu, E. D. Liu, M. I. Dykman, and A. Bachtold, Ultrasensitive force detection with a nanotube mechanical resonator, Nat. Nanotechnol. **8**, 493 (2013).
[9] P. Weber, J. Güttinger, I. Tsioutsios, D. E. Chang, and A. Bachtold, Coupling graphene mechanical resonators to superconducting microwave cavities, Nano Lett. **14**, 2854 (2014).
[10] V. Singh, S. J. Bosman, B. H. Schneider, Y. M. Blanter, A. Castellanos-Gomez, and G. Steele, Optomechanical

coupling between a multilayer graphene mechanical resonator and a superconducting microwave cavity, Nat. Nanotechnol. **9**, 820 (2014).

[11] A. Tavernarakis, J. Chaste, A. Eichler, G. Ceballos, M. C. Gordillo, J. Boronat, and A. Bachtold, Atomic Monolayer Deposition on the Surface of Nanotube Mechanical Resonators, Phys. Rev. Lett. **112**, 196103 (2014).

[12] Robin M. Cole, George A. Brawley, Vivekananda P. Adiga, Roberto De Alba, Jeevak M. Parpia, Bojan Ilic, Harold G. Craighead, and Warwick P. Bowen, Evanescent-Field Optical Readout of Graphene Mechanical Motion at Room Temperature, Phys. Rev. Applied **3**, 024004 (2015).

[13] Antoine Reserbat-Plantey, Kevin G. Schädler, Louis Gaudreau, Gabriele Navickaite, Johannes Güttinger, Darrick Chang, Costanza Toninelli, Adrian Bachtold, and Frank H. L. Koppens, Electromechanical control of nitrogen-vacancy defect emission using graphene NEMS, Nat. Commun. **7**, 10218 (2016).

[14] Chang-Hua Liu, In Soo Kim, and Lincoln J. Lauhon, Optical control of mechanical mode-coupling within a MoS_2 resonator in the strong-coupling regime, Nano Lett. **15**, 6727 (2015).

[15] P. R. Saulson, Thermal noise in mechanical experiments, Phys. Rev. D **42**, 2437 (1990).

[16] E. Majorana and Y. Ogawa, Mechanical thermal noise in coupled oscillators, Phys. Lett. A **233**, 162 (1997).

[17] M. Pinard, Y. Hadjar, and A. Heidmann, Effective mass in quantum effects of radiation pressure, Eur. Phys. J. D **7**, 107 (1999).

[18] K. Yamamoto, S. Otsuka, M. Ando, K. Kawabe, and K. Tsubono, Experimental study of thermal noise caused by an inhomogeneously distributed loss, Phys. Lett. A **280**, 289 (2001).

[19] L. Conti, M. De Rosa, F. Marin, L. Taffarello, and M. Cerdonio, Room temperature gravitational wave bar detector with optomechanical readout, J. Appl. Phys. **93**, 3589 (2003).

[20] See Supplemental Material at http://link.aps.org/supplemental/10.1103/PhysRevApplied.6.064021 for additional microfabrication, experimental and modelization details.

[21] Zheng Han, Amina Kimouche, Dipankar Kalita, Adrien Allain, Hadi Arjmandi-Tash, Antoine Reserbat-Plantey, Laëtitia Marty, Sébastien Pairis, Valérie Reita, Nedjma Bendiab, Johann Coraux, and Vincent Bouchiat, Homogeneous optical and electronic properties of graphene due to the suppression of multilayer patches during CVD on copper foils, Adv. Funct. Mater. **24**, 964 (2014).

[22] Antoine Reserbat-Plantey, Dipankar Kalita, Zheng Han, Laurence Ferlazzo, Sandrine Autier-Laurent, Katsuyoshi Komatsu, Chuan Li, Raphaël Weil, Arnaud Ralko, Laëtitia Marty, Sophie Guéron, Nedjma Bendiab, Hélène Bouchiat, and Vincent Bouchiat, Strain superlattices and macroscale suspension of graphene induced by corrugated substrates, Nano Lett. **14**, 5044 (2014).

[23] Jae-Ung Lee, Duhee Yoon, and Hyeonsik Cheong, Estimation of Young's modulus of graphene by Raman spectroscopy, Nano Lett. **12**, 4444 (2012).

[24] P. F. Cohadon, A. Heidmann, and M. Pinard, Cooling of a Mirror by Radiation Pressure, Phys. Rev. Lett. **83**, 3174 (1999).

[25] Robert A. Barton, Isaac R. Storch, Vivekananda P. Adiga, Reyu Sakakibara, Benjamin R. Cipriany, B. Ilic, Si Ping Wang, Peijie Ong, Paul L. McEuen, Jeevak M. Parpia, and Harold G. Craighead, Photothermal self-oscillation and laser cooling of graphene optomechanical systems, Nano Lett. **12**, 4681 (2012).

[26] A. Fartash, Ivan K. Schuller, and M. Grimsditch, Thin-film modeling for mechanical measurements: Should membranes be used or plates?, J. Appl. Phys. **71**, 4244 (1992).

[27] Maximilian J. Seitner, Katrin Gajo, and Eva M. Weig, Damping of metallized bilayer nanomechanical resonators at room temperature, Appl. Phys. Lett. **105**, 213101 (2014).

[28] Lukas Novotny, Strong coupling, energy splitting, and level crossings: A classical perspective, Am. J. Phys. **78**, 1199 (2010).

[29] G. Anetsberger, R. Riviere, A. Schliesser, O. Arcizet, and T. J. Kippenberg, Ultralow-dissipation optomechanical resonators on a chip, Nat. Photonics **2**, 627 (2008).

[30] Andreas Jöckel, Matthew T. Rakher, Maria Korppi, Stephan Camerer, David Hunger, Matthias Mader, and Philipp Treutlein, Spectroscopy of mechanical dissipation in micro-mechanical membranes, Appl. Phys. Lett. **99**, 143109 (2011).

[31] Yeghishe Tsaturyan, Andreas Barg, Anders Simonsen, Luis Guillermo Villanueva, Silvan Schmid, Albert Schliesser, and Eugene S. Polzik, Demonstration of suppressed phonon tunneling losses in phononic bandgap shielded membrane resonators for high-Q optomechanics, Opt. Express **22**, 6810 (2014).

[32] T. Larsen, S. Schmid, L. Grönberg, A. O. Niskanen, J. Hassel, S. Dohn, and A. Boisen, Ultrasensitive string-based temperature sensors, Appl. Phys. Lett. **98**, 121901 (2011).

[33] R. Kubo, The fluctuation-dissipation theorem, Rep. Prog. Phys. **29**, 255 (1966).

[34] C. Höhberger Metzger and K. Karrai, Cavity cooling of a microlever, Nature (London) **432**, 1002 (2004).

[35] A. Sampathkumar, T. W. Murray, and K. L. Ekinci, Photothermal operation of high frequency nanoelectromechanical systems, Appl. Phys. Lett. **88**, 223104 (2006).

[36] T. Caniard, P. Verlot, T. Briant, P.-F. Cohadon, and A. Heidmann, Observation of Back-Action Noise Cancellation in Interferometric and Weak Force Measurements, Phys. Rev. Lett. **99**, 110801 (2007).

[37] J. Laurent, A. Mosset, O. Arcizet, J. Chevrier, S. Huant, and H. Sellier, "Negative" Backaction Noise in Interferometric Detection of a Microlever, Phys. Rev. Lett. **107**, 050801 (2011).

[38] A. B. Shkarin, N. E. Flowers-Jacobs, S. W. Hoch, A. D. Kashkanova, C. Deutsch, J. Reichel, and J. G. E. Harris, Optically Mediated Hybridization between Two Mechanical Modes, Phys. Rev. Lett. **112**, 013602 (2014).

[39] Jan Gieseler, Bradley Deutsch, Romain Quidant, and Lukas Novotny, Subkelvin Parametric Feedback Cooling of a Laser-Trapped Nanoparticle, Phys. Rev. Lett. **109**, 103603 (2012).

[40] Antoine Reserbat-Plantey, Laetitia Marty, Olivier Arcizet, Nedjma Bendiab, and Vincent Bouchiat, A local optical probe for measuring motion and stress in a nanoelectromechanical system, Nat. Nanotechnol. **7**, 151 (2012).

[41] Thomas Faust, Johannes Rieger, Maximilian J. Seitner, Peter Krenn, Jörg P. Kotthaus, and Eva M. Weig, Nonadiabatic Dynamics of Two Strongly Coupled Nanomechanical Resonator Modes, Phys. Rev. Lett. **109**, 037205 (2012).

[42] A. Gloppe, P. Verlot, E. Dupont-Ferrier, A. Siria, P. Poncharal, G. Bachelier, P. Vincent, and O. Arcizet, Bidimensional nano-optomechanics and topological backaction in a non-conservative radiation force field, Nat. Nanotechnol. **9**, 920 (2014).

[43] B. Pigeau, S. Rohr, L. Mercier de Lépinay, A. Gloppe, V. Jacques, and O. Arcizet, Observation of a phononic Mollow triplet in a multimode hybrid spin-nanomechanical system, Nat. Commun. **6**, 8603 (2015).

[44] L. Mercier de Lépinay, B. Pigeau, B. Besga, P. Vincent, P. Poncharal, and O. Arcizet, A universal and ultrasensitive nanomechanical sensor for imaging 2D force fields, Nat. Nanotechnol., doi:10.1038/nnano.2016.193 (2016).

[45] K. R. Brown, C. Ospelkaus, Y. Colombe, A. C. Wilson, D. Leibfried, and D. J. Wineland, Coupled quantized mechanical oscillators, Nature (London) **471**, 196 (2011).

[46] H. Seok, L. F. Buchmann, E. M. Wright, and P. Meystre, Multimode strong-coupling quantum optomechanics, Phys. Rev. A **88**, 063850 (2013).

[47] Nicolas Spethmann, Jonathan Kohler, Sydney Schreppler, Lukas Buchmann, and Dan M. Stamper-Kurn, Cavity-mediated coupling of mechanical oscillators limited by quantum back-action, Nat. Phys. **12**, 27 (2016).

Supplementary information to: Optomechanical investigation of a hybrid graphene-nanoresonator system: deviation from the normal mode expansion

I. SAMPLE MICROFABRICATION

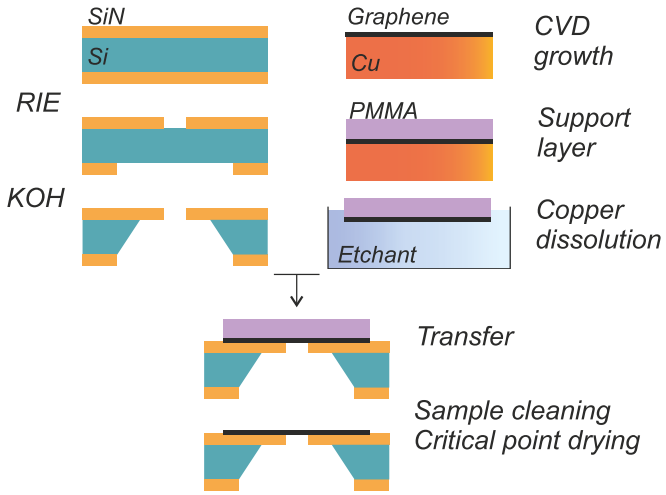

Figure S1: Sketch of the micro-fabrication sequence.

The used substrate is a silicon wafer coated on both sides with plasma-sputtered low stress Si_3N_4 thin films of 500 nm thickness. In a first lithography step, large windows (of about $100\,\mu m \times 150\mu m$) are defined on the wafer backside. A second laser lithography step on the top silicon nitride surface defines small square windows in the range between 4 to 25 μm side length centered above the large windows. The alignment of both lithography steps on each side is realized on the wafer periphery. The silicon nitride is etched away in the developed regions through the windows opened on both sides of the wafer by reactive ion etching in a sulphur hexafluoride SF_6 plasma. In order to permit optical transmission through the wafer, the silicon is subsequently etched away through the windows opened in the silicon nitride layers in a potassium hydroxide KOH solution. This results in suspended silicon nitride membranes with pre-defined holes as shown in Figure S1.
The graphene is grown on a copper foil by chemical vapor deposition (CVD) from a methane precursor to form a continuous layer (see ref. [1] for more details). The monolayer graphene is then spin-coated with a resist support layer (PMMA), the copper is etched away in a ammonium persulfate solution, and the graphene is transferred onto the pre-patterned substrate. After removal of the PMMA layer in acetone and rinsing in isopropanol, the sample is dried in a supercritical carbon dioxide dryer to protect it from strong surface tension forces that can be exerted by drying liquid droplets. Once these steps are accomplished, we obtain freely suspended graphene membranes supported by silicon nitride frame that is suspended itself.
In order to check the quality of the suspended graphene, we perform confocal micro-Raman mapping. Note that only information from the suspended regions can be extracted since the high fluorescence background of the silicon nitride hides the graphene related signatures in the supported regions. Figure S2a shows a typical Raman spectrum taken at the center of a $20 \times 20\,\mu m^2$ membrane. The absence of a significant D-peak confirms the high structural quality of the grown graphene. Figures S2b,S2c also show maps of the G and 2D-mode intensities, frequencies and widths obtained from Lorentzian fitting, which show a good spatial homogeneity. The average values for the G- and 2D-bands frequencies in the suspended regions are $1588.3\,cm^{-1}$ and $2676.5\,cm^{-1}$ respectively. Analyzing the respective frequencies of these modes according to reference [2] as shown in Fig. S2d, it is possible to extract strain and doping in the membrane. Both modes are hence slightly up-shifted with respect to the unperturbed graphene membrane, which can be explained in terms of low mechanical strain and hole doping in the order of 0.02% and $5 \cdot 10^{12}\,cm^{-2}$ respectively as can be deduced from figure 2d. These values are very small so that an effect of strain and charge doping on the optical properties of the graphene membrane can be safely excluded.

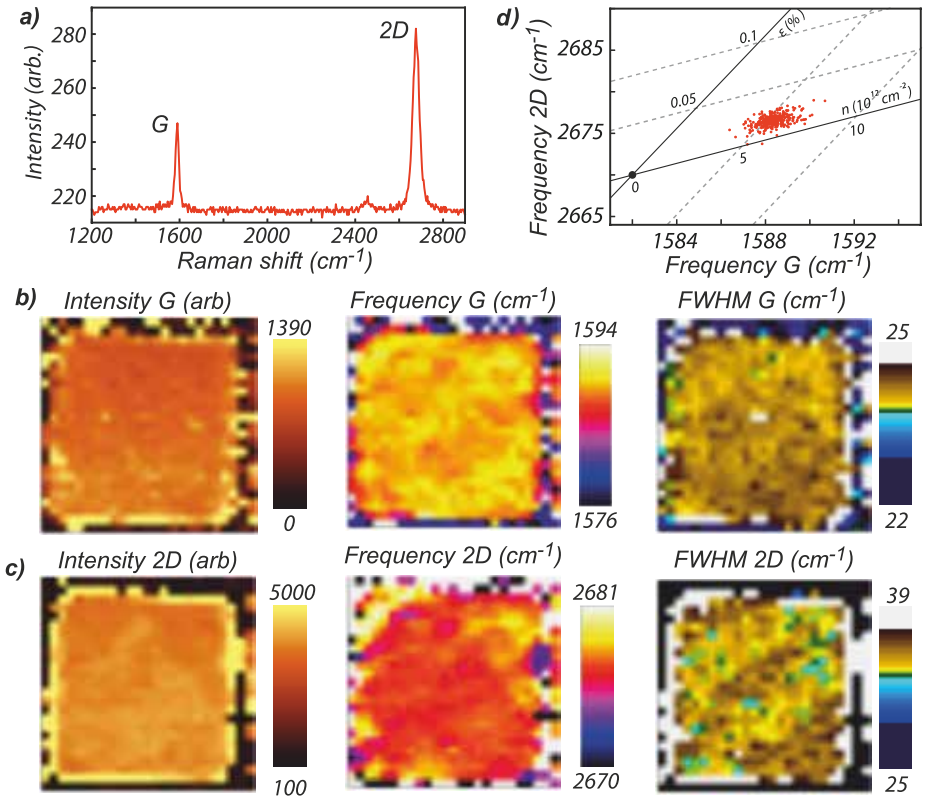

Figure S2: Characterization of suspended $20 \times 20\,\mu m^2$ graphene membrane by Raman spectroscopy. a) Typical spectrum ($1800\,cm^{-1}$ gratings, 532 nm). b) (and c) Raman mappings extracted from the G (resp2D) modes Lorentzian fitting. d) 2D versus G bands frequencies diagram and correspondence with strain and doping in graphene as proposed in [2].

II. EXPERIMENTAL DETAILS

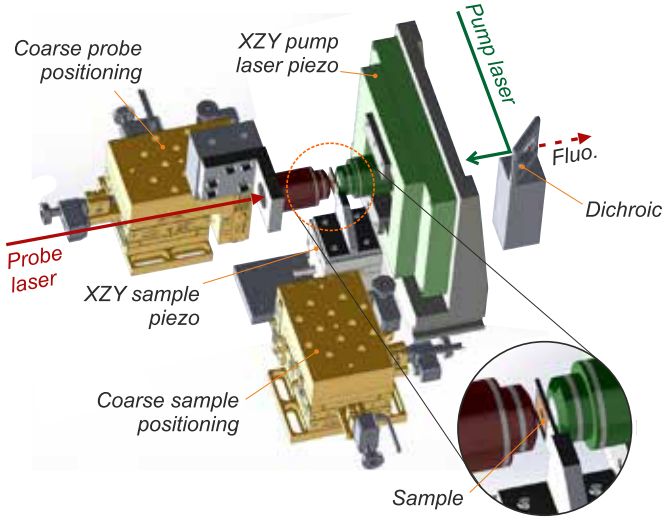

Figure S3: Sketch of inner part of the vacuum chamber.

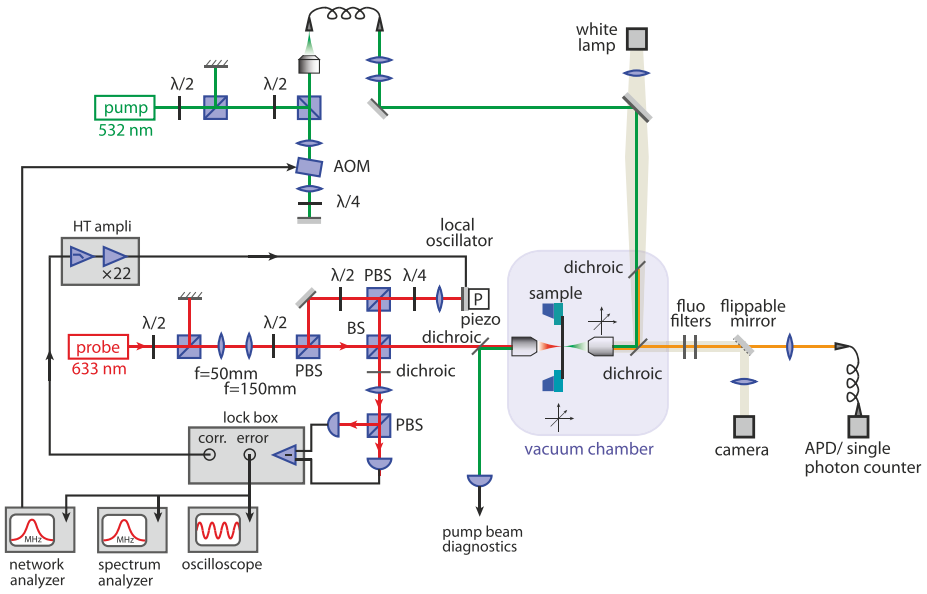

Figure S4: Sketch of the experiment. BS(PBS): (polarizing) beam splitter, AOM: acousto-optic modulator.

Schematics of the experiment are shown in Figure S3 and Figure S4. The sample is mounted vertically on a XYZ piezo stage (100x100x100μm scan range) permitting a precise positioning with respect to the probe laser beam, which is fixed in space in order to ensure a stable operation of the interferometer. The microscope objective which focusses the pump laser on the sample is mounted on a XYZ piezo stage (30x30x10μm scan range) in order to micro-position the actuation laser on the graphene surface. Two XYZ motorized translation stages permits a coarse positioning of this triple arrangement.

Microscope objective with long working distances (4 mm) and large numerical apertures (100x/0.75) are employed. They permit to focus the pump and probe beams down to optical waists of approximately 330 nm, with an half angle of the order of 45°. The KOH chemical etching angle of silicon (54°) which forms the bottom part of the sample permits to maintain the full transmission of the laser beams when positioned on the graphene membrane. The probe laser is injected from the bottom part of the sample.

The vacuum chamber has been designed to incorporate a large internal volume to host several massive translation stages, as well as numerous optical and electrical accesses. It is machined in a monolithic aluminum block and was anodized to maintain a high surface quality overtime. A 300 l/s turbopump allows to reach 1e-6 mbar under continuous pumping, but in order to avoid excessive vibrations, the pump is stopped during sensitive measurements. In that case, a static pressure below 1e-2 mbar can be maintained during several days.

The overall layout of the optical table is sketched in Figure S4. The laser source employed for fluorescence measurements and optomechanical actuation is a 532 nm diode pumped solid-state frequency doubled Nd:YaG laser. This low noise, single frequency laser was found appropriate to ensure a great pump intensity stability and presented weak intensity noise. A confocal microscope arrangement was implemented. Two injections path were also employed, a direct one, where the laser is only adjusted in size and polarization controlled, and a second one, where its intensity can be adjusted and modulated with an acousto-optic modulator (AOM). The latter is controlled with the output signal of a network analyzer for optical force excitation. The laser enters the vacuum chamber through an optical window covered with a broadband anti-reflection coating, it is reflected by a dichroic mirror located inside the cavity, so that the pump beam and fluorescence channel do not cross the same optical window, which could have increased the parasitic fluorescence. A white light source and a CCD camera can optionally be used for coarse alignment of the sample. The reflected pump intensity is collected through a 90/10 non polarizing beam splitter which is placed on the injection path, and focused on a fast and low noise detector. The transmitted pump intensity is collected by the probe laser injection objective, deflected by a second dichroic on a photodetector permitting to probe the sample transmission and measure the intensity modulation strength of the pump laser. The intensity modulation is realized by an acousto-optic modulator used in double path. In order to ensure a flat and broadband response, a careful spatial superposition of the two path is realized. A 50MHz bandwidth is achieved, with a large on/off rejection

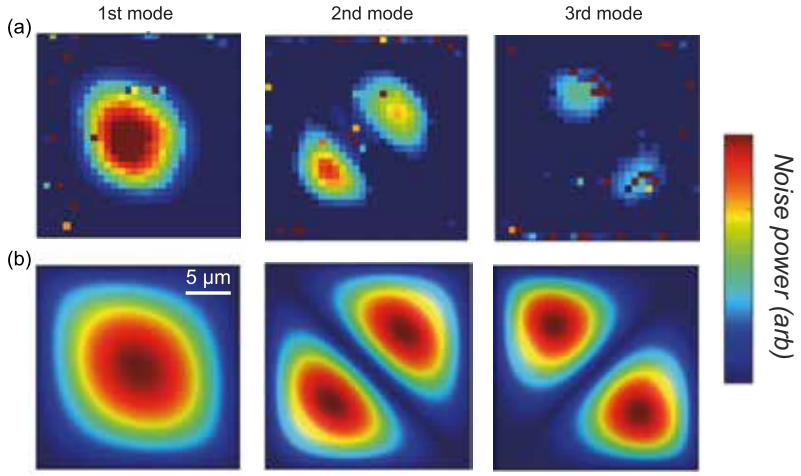

Figure S5: **Spatial profiles of the first three vibrational graphene modes** (a) Maps of the first three vibrational modes of a square membrane with a width of 20 μm obtained by probing the thermal noise amplitudes while scanning the sample position (30x30 points, optical waist of 400 nm). In each point the readout sensitivity is evaluated thanks to the reference calibration signal. The first mode is slightly elliptically shaped and the two other ones are aligned along the diagonals of the square. These properties can be explained in terms of strain along the diagonal that originates from the graphene transfer process. It splits the frequencies of the otherwise degenerate second vibrational mode. (b) This assumption is reproduced by finite element modeling for a membrane with initial strain along the diagonal.

(above 70 dB). The output of the AOM is filtered by a monomode fiber prior to its injection in the chamber.

The probe laser is a 15 mW Helium-Ne laser, which was verified to be shot noise limited over the whole measurement frequency range. A balanced homodyne detection is used to probe the phase fluctuations of the beam reflected on the sample. In addition to the actuation piezo, which is used to stabilize the interferometer, a fast piezo is mounted below the local oscillator mirror in order to calibrate the experiment. A fixed monochromatic modulation is applied, which generates a stable modulation of the interferometer (of a few pm), which is thus independent of reflectivity variations on the sample surface or spatial drifts that can occur in the chamber. In order to allow to change the polarization sent onto the sample, the reflected signal is deviated by a 90/10 non polarizing beam splitter, prior to its superposition on the local oscillator beam. The error signal of the balanced homodyne detection is split and sent on an oscilloscope for real time monitoring of the lock, on a spectrum analyzer for thermal noise measurements and on a network analyzer for response measurements The stability of the interferometer was good enough to realize large spatial maps (up to 100x100 points, lasting for up to 12h) without having to relock the interferometer (which can compensate for 3 μm drifts).

III. PHENOMENOLOGICAL MODEL

A. Dynamical equations

Here we give more details on the modelisation employed to analyze our observations. The dynamical equation of the coupled systems reads:

$$\begin{aligned} \ddot{\delta x_{\mathrm{G}}} &= -\Omega_{\mathrm{G}}^2\,(\delta x_{\mathrm{G}} - \delta x_{\mathrm{S}}) - \Gamma_{\mathrm{G}}\,(\dot{\delta x_{\mathrm{G}}} - \dot{\delta x_{\mathrm{S}}}) + \tfrac{\delta F_{\mathrm{G}}}{M_{\mathrm{G}}} \\ \ddot{\delta x_{\mathrm{S}}} &= -\Omega_{\mathrm{S}}^2\,\delta x_{\mathrm{S}} - \Gamma_{\mathrm{S}}\,\dot{\delta x_{\mathrm{S}}} + \mu\Omega_{\mathrm{G}}^2\,(\delta x_{\mathrm{G}} - \delta x_{\mathrm{S}}) + \mu\Gamma_{\mathrm{G}}\,(\dot{\delta x_{\mathrm{G}}} - \dot{\delta x_{\mathrm{S}}}) + \tfrac{\delta F_{\mathrm{S}}}{M_{\mathrm{S}}} \end{aligned} \tag{S1}$$

where Ω_{G}, Ω_{S} are the uncoupled resonant frequencies, $\Gamma_{\mathrm{S}}, \Gamma_{\mathrm{G}}$ the uncoupled damping rates. $\delta F_{\mathrm{G,S}}$ are external forces applied on the graphene membrane and silicon nitride nanoresonator respectively. M_G represents the effective mass of the graphene resonator at the measurement location, while $\mu \equiv M_G/M_S$ parameterize the hybridization strength which depends on the spatial overlaps between eigenmodes patterns. Intuitively if the graphene is positioned at a

node of the SiN eigenmode, their hybridization will be reduced. The dynamics of the system is described in Fourier space by $\begin{pmatrix} \delta x_{\rm G}[\Omega] \\ \delta x_{\rm S}[\Omega] \end{pmatrix} = \boldsymbol{\chi}[\Omega] \cdot \begin{pmatrix} \delta F_{\rm G}[\Omega] \\ \mu\, \delta F_{\rm S}[\Omega] \end{pmatrix}$ with $\delta x_i[\Omega] \equiv \int_{\mathbb{R}} dt e^{i\Omega t} \delta x_i(t)$. We have:

$$\boldsymbol{\chi}[\Omega]^{-1} \equiv M_{\rm G} \mathbf{Y}[\Omega] = M_{\rm G} \begin{pmatrix} \Omega_{\rm G}^2 - \Omega^2 - i\Omega\Gamma_{\rm G} & -\Omega_{\rm G}^2 + i\Omega\Gamma_{\rm G} \\ -\mu\Omega_{\rm G}^2 + i\Omega\mu\Gamma_{\rm G} & \Omega_{\rm S}^2 + \mu\Omega_{\rm G}^2 - \Omega^2 - i\Omega(\Gamma_{\rm S} + \mu\Gamma_{\rm G}) \end{pmatrix}. \tag{S2}$$

where we have introduced the dynamical matrix $\mathbf{Y}[\Omega]$. It can be expressed as:

$$\mathbf{Y}[\Omega] = \begin{pmatrix} Y_{\rm G} & -(Y_{\rm G} + \Omega^2) \\ -\mu(Y_{\rm G} + \Omega^2) & Y_{\rm S} + \mu(Y_{\rm G} + \Omega^2) \end{pmatrix}, \tag{S3}$$

using $Y_{\rm G,S} \equiv \Omega_{\rm G,S}^2 - \Omega^2 - i\Omega\Gamma_{\rm G,S}$. It can be diagonalized and its eigenmodes can be generally written:

$$Y_{\pm}[\Omega] = \Omega_{\pm}^2 - \Omega^2 - i\Omega\Gamma_{\pm}$$

The eigenvalues of the admittance matrix are:

$$Y_{\pm}[\Omega] = \frac{\Omega_+^2 + \Omega_-^2}{2} - \Omega^2 - i\Omega\frac{\Gamma_{\rm S} + (1+\mu)\Gamma_{\rm G}}{2} \pm \frac{1}{2}\sqrt{A[\Omega]}$$

with

$$A[\Omega] \equiv (\Omega_+^2 - \Omega_-^2)^2 - \Omega^2((\Gamma_{\rm S} - (1+\mu)\Gamma_{\rm G})^2 + 4\mu\Gamma_{\rm S}\Gamma_{\rm G}) - 2i\Omega(\Omega_{\rm S}^2\Gamma_{\rm S} + (1+\mu)^2\Omega_{\rm G}^2\Gamma_{\rm G} + (\mu-1)(\Omega_{\rm S}^2\Gamma_{\rm G} + \Omega_{\rm G}^2\Gamma_{\rm S}))$$

B. Eigenmodes

Diagonalizing the restoring force matrix

$$\mathbf{Y}[0] = M_{\rm G}^{-1}\boldsymbol{\chi}[0]^{-1} = \begin{pmatrix} \Omega_{\rm G}^2 & -\Omega_{\rm G}^2 \\ -\mu\Omega_{\rm G}^2 & \Omega_{\rm S}^2 + \mu\Omega_{\rm G}^2 \end{pmatrix}$$

yields the new eigenfrequencies $\Omega_{\pm}/2\pi$ of the coupled system:

$$\Omega_{\pm}^2 \equiv \frac{(1+\mu)\Omega_{\rm G}^2 + \Omega_{\rm S}^2}{2} \pm \frac{1}{2}\sqrt{\left(\Omega_{\rm S}^2 - (1+\mu)\Omega_{\rm G}^2\right)^2 + 4\mu\Omega_{\rm G}^2\Omega_{\rm S}^2}. \tag{S4}$$

Assuming that the SiN mode has a fixed frequency, the maximum frequency splitting is achieved for a graphene mode frequency of $\Omega_{\rm G}^0$ given by

$${\Omega_{\rm G}^0}^2 = \Omega_{\rm S}^2\frac{1-\mu}{(1+\mu)^2}$$

and amounts to:

$$\Omega_+^2 - \Omega_-^2\big|_{\rm min} = \Omega_S^2\left(\frac{4\mu}{(1+\mu)^2}\right)^{1/2} \approx 2\Omega_{\rm S}^2\sqrt{\mu}$$

so that for small μ, the minimum relative frequency splitting is $\sqrt{\mu}$.

The diagonalization also yields the new eigenmodes $\mathbf{e}_{\pm}$ of the coupled system. They can be expressed as:

$$\mathbf{e}_{\pm} = \begin{pmatrix} \Omega_{\rm G}^2 \\ \Omega_{\rm G}^2 - \Omega_{\pm}^2 \end{pmatrix} \frac{1}{\sqrt{(\Omega_{\rm G}^2 - \Omega_{\pm}^2)^2 + \Omega_{\rm G}^4}} \tag{S5}$$

This expression permits identifying the upper (lower) mode as the anti-symmetric (symmetric) one since the coefficient $\Omega_{\rm G}^2 - \Omega_{\pm}^2$ has different sign for each eigenmode (see Figure S6). As defined, the eigenvectors are not orthogonal, this is a consequence of the mass asymmetry. As expected for the dynamics describe here, which derives from a potential energy, in case of identical masses ($\mu = 1$), the restoring force matrix becomes symmetric and the eigenvectors are orthogonal.

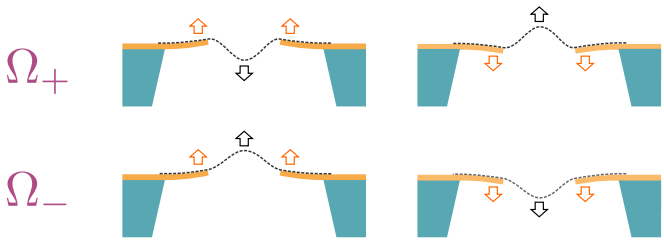

Figure S6: Sketch of the spatial profiles of the coupled eigenvectors $\mathbf{e}_\pm$. The lowest energetic mode is the symmetric one.

C. Effective damping rates

The effective damping rates $\Gamma_\pm$ of the coupled modes are mathematically defined as $\Gamma_\pm = -\mathrm{Im}(Y_\pm[\Omega_\pm])/\Omega_\pm$ but their derivation is more convenient using the following expressions:

$$\Gamma_+ + \Gamma_- = -\mathrm{Im}\frac{(Y_+[\Omega_+] + Y_-[\Omega_+])}{\Omega_+} \quad \text{and} \quad \Gamma_+ - \Gamma_- = -\mathrm{Im}\frac{(Y_+[\Omega_+] - Y_-[\Omega_+])^2}{2\Omega_+(\Omega_+^2 - \Omega_-^2)}$$

so that $\Gamma_+ + \Gamma_- = \Gamma_\mathrm{S} + (1+\mu)\Gamma_\mathrm{G}$ and $\Gamma_+ - \Gamma_- = \frac{\Gamma_\mathrm{S}\Omega_\mathrm{S}^2 + (1+\mu)^2\Omega_\mathrm{G}^2\Gamma_\mathrm{G} + (\mu-1)(\Gamma_\mathrm{S}\Omega_\mathrm{G}^2 + \Gamma_\mathrm{G}\Omega_\mathrm{S}^2)}{\Omega_+^2 - \Omega_-^2}$. Then:

$$\Gamma_\pm = \frac{\Gamma_\mathrm{S} + (1+\mu)\Gamma_\mathrm{G}}{2} \pm \frac{\Gamma_\mathrm{S}\Omega_\mathrm{S}^2 + (1+\mu)^2\Omega_\mathrm{G}^2\Gamma_\mathrm{G} + (\mu-1)(\Gamma_\mathrm{S}\Omega_\mathrm{G}^2 + \Gamma_\mathrm{G}\Omega_\mathrm{S}^2)}{2(\Omega_+^2 - \Omega_-^2)}$$

Using the previous expression, and the expression for the minimum frequency splitting, it is then possible in case of identical damping rates $\Gamma_\mathrm{G} = \Gamma_\mathrm{S} \equiv \Gamma$ to put an upper bound on the damping asymmetry of coupled modes, at the level of $\Gamma_+ - \Gamma_- < \Gamma\sqrt{\mu} \ll \Gamma$.

D. Normal mode expansion

The normal mode expansion consists in attributing one independent Langevin force to each mechanical eigenmode so that the thermal noise spectrum $S_{\delta x_\mathrm{G}}[\Omega]$ should be fitted with [3] :

$$\sum_{m=\pm} A_\pm \left| \frac{1}{\Omega_\pm^2 - \Omega^2 - i\Omega\Gamma_\pm} \right|^2$$

with positive fitting parameters $A_\pm, \Gamma_\pm$ and $\Omega_\pm$ This expression does not allow to describe the measured thermal noise spectra presenting noise reduction that cannot be adjusted with two mechanical thermal noise spectra.

E. Thermal noise

Based on the fluctuation dissipation theorem, we compute the theoretical local mechanical susceptibility $\chi_\mathrm{GG}[\Omega]$ by inverting equation (S2) and picking out the graphene-graphene component: $\delta x_\mathrm{G} = \chi_\mathrm{GG}\,\delta F_\mathrm{G}$:

$$\chi_\mathrm{GG}[\Omega] = \frac{1}{M_\mathrm{G}}\frac{1}{\det\mathbf{Y}[\Omega]}\left(Y_\mathrm{S} + \mu(Y_\mathrm{G} + \Omega^2)\right)$$

Using $\det\mathbf{Y}[\Omega] = Y_\mathrm{G}Y_\mathrm{S} - \mu\Omega^2(Y_\mathrm{G} + \Omega^2)$ yields the following expression:

$$\frac{1}{\chi_\mathrm{GG}} = \frac{1}{\chi_G} - \frac{(\chi_G^{-1} + M_\mathrm{G}\Omega^2)^2}{\chi_\mathrm{S}^{-1} + \chi_\mathrm{G}^{-1} + M_\mathrm{G}\Omega^2} \tag{S6}$$

and

$$\chi_{\mathrm{GG}}[\Omega] = \frac{1}{M_{\mathrm{G}}} \frac{\Omega_{\mathrm{S}}^2 + \mu\Omega_{\mathrm{G}}^2 - \Omega^2 - i\Omega\left(\Gamma_{\mathrm{S}} + \mu\Gamma_{\mathrm{G}}\right)}{\Omega^4 - \Omega^2\left(\Omega_{\mathrm{G}}^2 + \Omega_{\mathrm{S}}^2 + \mu\Omega_{\mathrm{G}}^2 + \Gamma_{\mathrm{G}}\Gamma_{\mathrm{S}}\right) + \Omega_{\mathrm{S}}^2\Omega_{\mathrm{G}}^2 - i\Omega\left(\Gamma_{\mathrm{G}}\Omega_{\mathrm{S}}^2 + \Gamma_{\mathrm{S}}\Omega_{\mathrm{G}}^2 - \Omega^2\left(\Gamma_{\mathrm{G}} + \Gamma_{\mathrm{S}} + \mu\Gamma_{\mathrm{G}}\right)\right)} \tag{S7}$$

This expression serves to adjust the response measurements. In case of an infinitely massive SiN resonator, the above expression converges towards the graphene susceptibility alone. At zero frequency, one has:

$$\chi_{\mathrm{GG}}[0] = \frac{1}{M_{\mathrm{G}}}\left(\frac{1}{\Omega_{\mathrm{G}}^2} + \frac{\mu}{\Omega_{\mathrm{S}}^2}\right) \tag{S8}$$

which is well approximated by the static graphene susceptibility in our situation ($\mu \ll 1$). The imaginary part of χ_{GG} permits estimating the spectral density of the thermal noise of the system measured on the graphene membrane, by using the fluctuation dissipation theorem: $S_{\delta x_{\mathrm{G}}}[\Omega] = \frac{2k_BT}{|\Omega|}\left|\mathrm{Im}\chi_{GG}[\Omega]\right|$, where the spectral density is defined according to the convention: $\langle\delta x[\Omega]\delta x[\Omega']\rangle = 2\pi\delta(\Omega+\Omega')S_x[\Omega]$. We have:

$$S_{\delta x_{\mathrm{G}}}[\Omega] = \frac{2k_BT}{M_{\mathrm{G}}} \frac{\Omega^4\Gamma_{\mathrm{G}} + \Omega^2\left(\Gamma_{\mathrm{G}}\Gamma_{\mathrm{S}}^2 + \mu\Gamma_{\mathrm{S}}\Gamma_{\mathrm{G}}^2 - 2\Gamma_{\mathrm{G}}\Omega_{\mathrm{S}}^2\right) + \Gamma_{\mathrm{G}}\Omega_{\mathrm{S}}^4 + \mu\Gamma_{\mathrm{S}}\Omega_{\mathrm{G}}^4}{\left(\Omega^4 - \Omega^2\left(\Omega_{\mathrm{G}}^2 + \Omega_{\mathrm{S}}^2 + \mu\Omega_{\mathrm{G}}^2 + \Gamma_{\mathrm{G}}\Gamma_{\mathrm{S}}\right) + \Omega_{\mathrm{S}}^2\Omega_{\mathrm{G}}^2\right)^2 + \Omega^2\left(\Gamma_{\mathrm{G}}\Omega_{\mathrm{S}}^2 + \Gamma_{\mathrm{S}}\Omega_{\mathrm{G}}^2 - \Omega^2\left(\Gamma_{\mathrm{G}} + \Gamma_{\mathrm{S}} + \mu\Gamma_{\mathrm{G}}\right)\right)^2}$$

This expression serves to fit the measured thermal noise.

F. Deviation from the normal mode expansion

In case of identical uncoupled eigenfrequencies ($\Omega_{\mathrm{S}} = \Omega_{\mathrm{G}}$), it is possible to compute the error made when trying to estimate the thermal noise with the normal mode expansion expression. The error is frequency dependent and maximum at the noise squashing frequency, where the thermal noise is found to be lower than the value originating from the normal mode expansion by a factor of $\left(1 + \Gamma_{\mathrm{S}}/\Gamma_{\mathrm{S}}\right)/2$ (no error is made in case of identical damping rates). This expression is independent on the coupling parameter μ as long as the anticrossing visibility is preserved: $\Gamma_{\pm} < \Omega_{+} - \Omega_{-}$ and can reach large values in case of strong damping heterogeneity. The maximum observed deviation almost reached 20 dB.

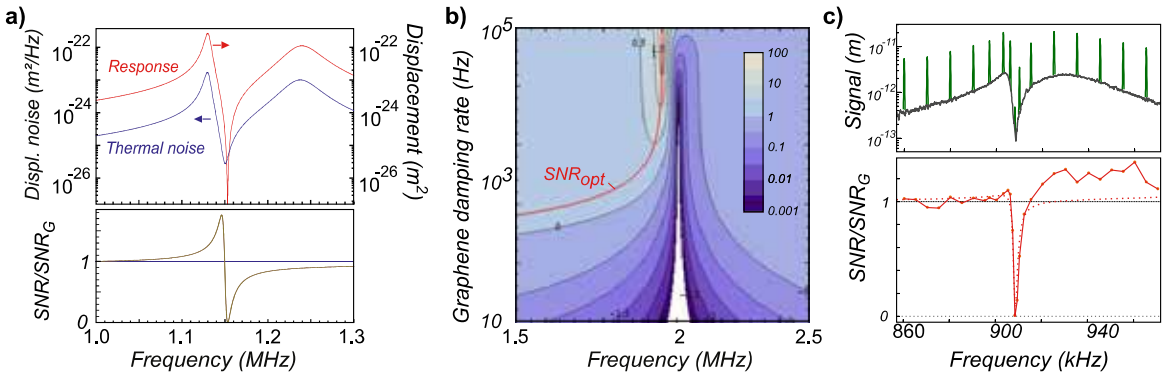

Figure S7: **Improvement of the SNR.** Left: above: Thermal noise spectrum and response measurement (in m^2) simulated using the model with $\mu = 0.005$, $\Omega_{\mathrm{G}}/2\pi = 1216\,\mathrm{kHz}$, $\Omega_{\mathrm{S}}/2\pi = 1150\,\mathrm{kHz}$, $\Gamma_{\mathrm{S}}/2\pi = 500\,\mathrm{Hz}$, $\Gamma_{\mathrm{G}}/2\pi = 50\,\mathrm{kHz}$, $M_g = 10^{-14}\,\mathrm{kg}$, $T = 300\,\mathrm{K}$ and a force amplitude of 5 fN; below: relative SNR increase (when compared to the graphene alone) as a function of the measurement frequency. Center: Map of the relative SNR increase dependency on the graphene damping rate. The red line represents the optimum SNR increase. Plotting parameters are $\mu = 0.1$, $\Gamma_{\mathrm{S}}/2\pi = 500\,Hz$, $\Omega_{\mathrm{S}}/2\pi = 1.5\,\mathrm{MHz}$. Right: above: experimental data showing the equivalent displacement measured with a 100 Hz resolution bandwidth, of the thermal noise spectrum alone in blue, and with an ensemble of monochromatic drive tones (green). The deduced signal-to-noise ratio is shown bellow, after a proper renormalizaton by the graphene alone contribution. The dashed red line represents the relative SNR change expected from the 2 modes phenomenological model. The deviation observed at large frequency is due to the presence of second higher order SiN mode presenting a larger coupling rate (but not accessible via thermal tuning). The modest, $\approx 10\%$, SNR increase observed in the vicinity of Ω_{S} could be largely increased with optimized parameters.

G. Signal-to-noise ratio in a force measurement

When applying a monochromatic force on the graphene with amplitude $\delta F_{\rm G}$ at frequency Ω, the measured displacement is $\delta x_{\rm G} = \chi_{\rm GG}\,\delta F_{\rm G}$ so that the signal to noise ratio of the measurement is

$$\mathrm{SNR}[\Omega] = \frac{|\chi_{\rm GG}[\Omega]|^2\,\delta F_{\rm G}^2}{\frac{2k_BT}{|\Omega|}\,|\mathrm{Im}\chi_{\rm GG}[\Omega]|},$$

which can be expressed as :

$$\mathrm{SNR}[\Omega] = \frac{\delta F_{\rm G}^2}{2M_{\rm G}\Gamma_{\rm G}k_BT}\,\frac{\left(\Omega_{\rm S}^2+\mu\Omega_{\rm G}^2-\Omega^2\right)^2+\Omega^2\left(\Gamma_{\rm S}+\mu\Gamma_{\rm G}\right)^2}{\Omega^4+\Omega^2\left(\Gamma_{\rm S}^2+\mu\Gamma_{\rm S}\Gamma_{\rm G}-2\Omega_{\rm S}^2\right)+\Omega_{\rm S}^4+\Omega_{\rm G}^4\mu\Gamma_{\rm S}/\Gamma_{\rm G}} \tag{S9}$$

The first fraction, called $\mathrm{SNR}_{\rm G}$ in the following, represents the SNR of the graphene membrane alone, where the spectral density of the Langevin force acting on graphene $2M_{\rm G}\Gamma_{\rm G}k_BT$ is compared to the power of the force signal δF^2. The second fraction represents the variation of SNR due to the hybridization to the SiN nanoresonator. Interestingly it can be larger than one in case of strong hybridization strength (large μ) and good SiN quality factor (small $\Gamma_{\rm S}$). In case of identical damping rates, the SNR can only smaller than one. The highest increase in SNR is obtained for $\Omega_{\rm opt}$ given by:

$$\Omega_{\rm opt} = \sqrt{\Omega_{\rm S}^2 - \frac{\Gamma_{\rm S}}{\Gamma_{\rm G}}\Omega_{\rm G}^2}$$

which is always defined in our experimental conditions ($\Gamma_{\rm S}/\Gamma_{\rm G} < 1/10$) and simply amounts to:

$$\mathrm{SNR}_{\rm opt}/\mathrm{SNR}_{\rm G} = 1 + \frac{\Gamma_{\rm G}}{\Gamma_{\rm S}}\mu.$$

In our situation we can expect a 50 % increase when working relatively far away from the anticrossing. More generally, this suggests that the SNR increase will be larger when hybridizing with high-Q SiN modes, presenting a large coupling strength μ. This SNR increase will be more profitable for low-Q graphene membranes. Figure S7 illustrate the dependence of the relative SNR increase on the system parameters. This modification of the SNR is also observed experimentally, see Figure S7 with a strong frequency dependence and a more complex spectral shape due to the interplay of several SiN modes. The modest improvement observed could be significantly improved with optimized mechanical parameters.

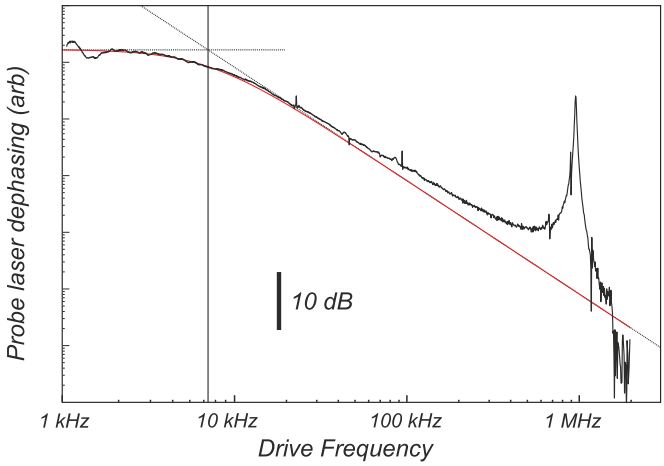

Figure S8: **Broadband response of the system.** In addition to the resonant mechanical response, visible at 1 MHz, also appear a low frequency response which is well adjusted with a first order low pass filter (cutoff: 7 kHz). It can be due to both a temperature mediated reflectivity change or to a thermally induced non-resonant mechanical deformation, but both possibilities reflects the thermal behavior of the membrane. The cutoff frequency represents the inverse propagation time of the driven heat wave to spread from the graphene center to the SiN rim. It permits estimating the heat diffusion coefficient for graphene, of the order of $\approx 10^{-6}\,\mathrm{m}^2/\mathrm{s}$. The slight deviation observed around 1 kHz is due to the lock of the interferometer, which tries to compensate the driven dephasing.

IV. BROADBAND RESPONSE

A broadband response is shown in Figure S8. A 2D numerical simulation has been developed in order to evaluate the thermal steady state of the system in presence of a monochromatic deposited heat modulation localized in the middle of the graphene membrane. From this modelization, the cutoff frequency, measured at the level of 7 kHz can be employed to derive the thermal diffusion coefficient. Then, the thermal resistance of the system can be computed numerically, by evaluating the temperature gradient across the sample in case of a low frequency modulation. The obtained value is 0.25 K per μW absorbed. It is important to mention that the 7 kHz cutoff corresponds to inverse propagation time of the thermal wave up to the SiN frame, located 10 μW away. As a consequence, when we intensity modulate the pump beam at 1200 kHz to realize resonant optical actuation of the mode, the thermal wave spreads over 700 nm, which is slightly larger than the optical waist, but significantly smaller than the characteristic dimensions of the mode profile. As such, it is justified to consider the thermal actuation mechanism as being confined under the optical spot and thus giving access to the local mechanical susceptibility.

[1] Han, Z. *et al.* Homogeneous optical and electronic properties of graphene due to the suppression of multilayer patches during CVD on copper foils. *Advanced Functional Materials* **24**, 964–970 (2014).

[2] Lee, J.-U., Yoon, D. & Cheong, H. Estimation of Young's modulus of graphene by Raman spectroscopy. *Nano Letters* **12**, 4444–8 (2012).

[3] Pinard, M., Hadjar, Y. & Heidmann, A. Effective mass in quantum effects of radiation pressure. *Eur. Phys. J. D* **7**, 107–116 (1999).